JPE 17-6-11

https://doi.org/10.6113/JPE.2017.17.6.1500
ISSN(Print): 1598-2092 / ISSN(Online): 2093-4718

Analysis and Control of NPC-3L Inverter Fed Dual Three-Phase PMSM Drives Considering their Asymmetric Factors

Jian Chen*, Zheng Wang†, Yibo Wang*, and Ming Cheng*

*,†School of Electrical Engineering, Southeast University, Nanjing, China

Abstract

The purpose of this paper is to study a high-performance control scheme for neutral-point-clamping three-level (NPC-3L) inverter fed dual three-phase permanent magnet synchronous motor (PMSM) drives by considering some asymmetric factors such as the non-identical parameters in phase windings. To implement this, the system model is analyzed for dual three-phase PMSM drives with asymmetric factors based on the vector space decomposition (VSD) principle. Based on the equivalent circuits, PI controllers with feedforward compensation are used in the *d-q* subspace for regulating torque, where the cut-off frequency of the PI controllers are set at the twice the fundamental frequency for compensating both the additional DC component and the second order component caused by asymmetry. Meanwhile, proportional resonant (PR) controllers are proposed in the *x-y* subspace for suppressing the possible unbalanced currents in the phase windings. A dual three-phase space vector modulation (DT-SVM) is designed for the drive, and the balancing factor is designed based on the numerical fitting surface for balancing the DC link capacitor voltages. Experimental results are given to demonstrate the validity of the theoretical analysis and the proposed control scheme.

Key words: Asymmetric factors, Neutral-point-clamping three-level inverter, PMSM drives, Space vector modulation, Vector space decomposition

I. INTRODUCTION

Multiphase motor drives offer some attractive features such as an increased system power, reduced torque ripple, excellent fault tolerant characteristic and high reliability [1]-[4]. On the other hand, the use of standard "off-the-shelf" components makes it necessary to select the phase number as a multiple of three, and it is preferable to use multiphase systems composed of three-phase subsystems [5]. Consequently, dual three-phase motor drives are attracting more attentions these days. By designing two sets of three-phase windings shifted by 30 electrical degrees, the $6k$th (k=1,2…) order pulsating torque component can be completely eliminated [6], [7]. Previously, a lot of research has been presented for dual three-phase motor drives. For controlling dual three-phase drives, one solution is based on dual synchronous frames and the electric motor is controlled separately in two three-phase subsystem [8], [9]. Another solution is based on vector space decomposition (VSD), where the fundamental components, harmonic components and zero-sequence components are decoupled and mapped onto three subspaces, namely α-β, *x-y* and z_1-z_2, which are orthogonal to each other [10]. The electromechanical torque is regulated in the α-β subspace and the harmonic components are suppressed to be zero in the *x-y* subspace by designing the modulation strategy. Meanwhile, the control in the z_1-z_2 subspace can generally be neglected by isolating the neutral points of two sets of windings. In [11], an additional control strategy is proposed in the *x-y* subspace for further suppression of the harmonic current. In [12], decoupling control is proposed in the fundamental subspace based on the VSD frame to improve the dynamic performance of dual three-phase PMSM drives. Furthermore, the control of a dual three-phase motor is considered for asymmetric operation in [13], [14], where the unbalanced components are mapped

Manuscript received Aug. 29, 2016; accepted Jun. 28, 2017
Recommended for publication by Associate Editor Younghoon Cho.
†Corresponding Author: zwang@eee.hku.hk
Tel: +86-25-83794169-803,Fax: +86-25-83791696, Southeast University
*School of Electrical Engineering, Southeast University, China

onto the harmonic subspace (*x*-*y* subspace) with the fundamental frequency, and improved PI controllers are proposed for eliminating the unbalanced current components. In addition, some of the control strategies and algorithms for traditional three-phase motor drives such as direct torque control and nonlinear control algorithm have been adapted for dual three-phase motor drives [15]-[20].

It should be noted that all of the aforementioned research is discussed based on two-level multiphase inverter fed drives. This blocks extensive application of multiphase motor drives in medium voltage drives. During the past two decades, a series of multilevel inverters topologies have been shown to exhibit excellent advantages in medium-voltage and high-voltage drives [21]. In addition, the neutral-point-clamping (NPC) type multilevel topology has become a popular configuration in the industry [22]. Therefore, NPC multilevel inverter fed multiphase motor drives have significant value in applications of high-power medium-voltage drives. SVM strategies based on the VSD principle have been proposed for NPC three-level NPC-3L five-phase induction motor drives in [23], [24] and for NPC-3L seven-phase induction motor drives in [25], where the optimum voltage vectors are chosen to synthesize the reference voltage in the α-β subspace while eliminating the voltage components in the harmonic subspace. However, all of the previous studies on multilevel inverters have been applied to open-loop controlled five-phase or seven-phase induction motor drives with symmetrical operation. Work on a closed-loop control scheme for multilevel dual three-phase PMSM drives considering asymmetric factors is still rare. Furthermore, SVM based on the VSD principle cannot be used for eliminating the unbalanced currents of dual three-phase drives with asymmetrical operation. This is due to the fact that it is very difficult to output specified components on the harmonic subspace except zero.

Unlike previous research, the purpose of this paper is to analyze and control NPC-3L inverter fed dual three-phase PMSM drives by considering asymmetric factors. In this paper, the VSD model of a dual three-phase PMSM with asymmetrical operation will be built and the dual three-phase SVM (DT-SVM) strategy is designed for NPC-3L inverters. According to the motor model and the modulation strategy, the vector control scheme based on the VSD is proposed for NPC-3L inverter fed dual three-phase PMSM drives. In the proposed VSD current control scheme, feedforward decoupling control and proportional resonant (PR) control are adopted to improve the dynamic performance of the drives and to suppress the unbalanced currents induced from some asymmetric factors such as the non-identical parameters between dual windings. In addition, a balanced factor is introduced for the DT-SVM to effectively balance the DC-link capacitor voltages, which are selected in term of the numerical fitting surface. Experiments are presented to verify the validity of the analysis and the proposed control scheme.

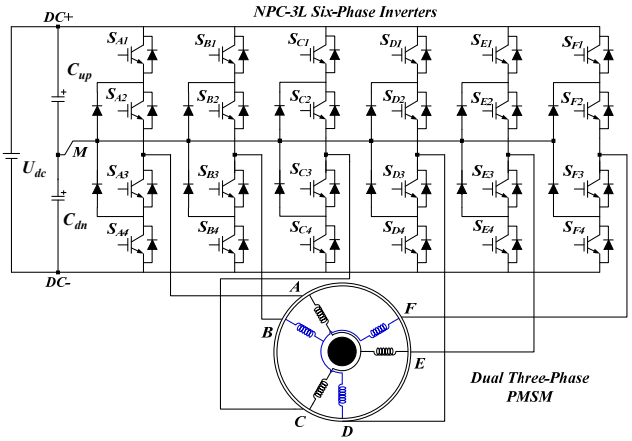

Fig. 1. Configuration of a NPC-3L inverter fed dual three-phase PMSM.

II. Configuration and Modeling

Fig. 1 shows the configuration of NPC-3L six-phase inverter fed dual three-phase PMSM drives, where the electric machine (also called an asymmetric six-phase PMSM) consists of two sets of three-phase Y type windings shifted by 30 electrical degrees. The neutral points of the two three-phase windings are isolated, and the dual three-phase PMSM is fed by NPC-3L six-phase inverters. Each phase of the NPC-3L inverter can output three-level polar voltages, which are $U_{dc}/2$, 0 and $-U_{dc}/2$. The three-level dual three-phase PMSM drives topology inherits the advantages of multiphase motors and multilevel inverters. It also offers attractive solutions for medium-voltage high-power drives.

Assuming that the windings are distributed sinusoidally, the permanent magnet (PM) flux is constant, the back EMFs are sinusoidal, and the magnetic saturation, magnetic hysteresis and mutual leakage inductance are neglected. The voltage and flux equations in the phase frame are as follows:

$$\begin{cases} \boldsymbol{u}_S = R_s \boldsymbol{i}_S + p\boldsymbol{\psi}_S \\ \boldsymbol{\psi}_S = \boldsymbol{L}_s \boldsymbol{i}_S + \psi_f \boldsymbol{F}(\theta) \end{cases} \tag{1}$$

where $\boldsymbol{u}_s$=[u_A, u_B, u_C, u_D, u_E, u_F,]^T is the stator voltage vector, $\boldsymbol{i}_s$=[i_A, i_B, i_C, i_D, i_E, i_F,]^T is the stator current vector, and $\boldsymbol{\psi}_s$ =[ψ_A, ψ_B, ψ_C, ψ_D, ψ_E, ψ_F,]^T is stator flux vector. ψ_f is the peak value of the PM flux, $\boldsymbol{F}(\theta)$=[cos(θ), cos(θ–π/6), cos(θ–2π/3), cos(θ–5π/6), cos(θ–4π/3), cos(θ–3π/2)] ^{T} is the rotated coefficient matrix, and θ is the rotor electrical degree. p is the differential operator d/dt, R_S is the stator resistor, and the stator inductance matrix is expressed as:

$$\boldsymbol{L}_s = \boldsymbol{A} + \boldsymbol{B} + L_{ls}\boldsymbol{I}_6 \tag{2}$$

where $\boldsymbol{I}_6$ is the identity matrix and L_{ls} is the leakage inductance.

$$\boldsymbol{A}=L_{sm}\begin{bmatrix} A_1 & A_2 & -A_3 & -A_2 & -A_3 & 0 \\ A_2 & A_1 & 0 & -A_3 & -A_2 & -A_3 \\ -A_3 & 0 & A_1 & A_2 & -A_3 & -A_2 \\ -A_2 & -A_3 & A_2 & A_1 & 0 & -A_3 \\ -A_3 & -A_2 & -A_3 & 0 & A_1 & A_2 \\ 0 & -A_3 & -A_2 & -A_3 & A_2 & A_1 \end{bmatrix} \tag{3}$$

where A_1=1, $A_2=\sqrt{3}/2$, A_3=1/2 and L_{sm} is the peak value of the main self-inductance.

$$\mathbf{B}=L_{rm}\begin{bmatrix} B_1 & B_2 & B_3 & B_4 & B_5 & B_6 \\ B_2 & -B_5 & B_4 & -B_1 & B_6 & -B_3 \\ B_3 & B_4 & B_5 & B_6 & B_1 & B_2 \\ B_4 & -B_1 & B_6 & -B_3 & B_2 & -B_5 \\ B_5 & B_6 & B_1 & B_2 & B_3 & B_4 \\ B_6 & -B_3 & B_2 & -B_5 & B_4 & -B_1 \end{bmatrix} \tag{4}$$

where $B_1=\cos(2\theta)$, $B_2=\cos(2\theta-\pi/6)$, $B_3=\cos(2\theta-2\pi/3)$, $B_4=\cos(2\theta-5\pi/6)$, $B_5=\cos(2\theta-4\pi/3)$, $B_6=\cos(2\theta-3\pi/2)$ and L_{rm} is the peak value of the reluctance inductance.

$$\boldsymbol{T}_{VSD}=\frac{1}{3}\begin{bmatrix} 1 & \sqrt{3}/2 & -1/2 & -\sqrt{3}/2 & -1/2 & 0 \\ 0 & 1/2 & \sqrt{3}/2 & 1/2 & -\sqrt{3}/2 & -1 \\ 1 & -\sqrt{3}/2 & -1/2 & \sqrt{3}/2 & -1/2 & 0 \\ 0 & 1/2 & -\sqrt{3}/2 & 1/2 & \sqrt{3}/2 & -1 \\ 1 & 0 & 1 & 0 & 1 & 0 \\ 0 & 1 & 0 & 1 & 0 & 1 \end{bmatrix} \tag{5}$$

$$\boldsymbol{T}_{park}=\begin{bmatrix} \cos\theta & \sin\theta \\ -\sin\theta & \cos\theta \end{bmatrix} \tag{6}$$

According to the VSD theory for dual three-phase machines [10], the original six-dimensional variables are decomposed onto three orthogonal subspaces α-β, x-y and z_1-z_2 by the VSD transformation matrix (5). The fundament and harmonic components with orders of 6m±5 (m=1,3,5···) are mapped on the α-β subspace, the harmonic components with orders of 6m±1 (m=1,3,5···) are mapped on the x-y subspace, and the zero-order components with orders of 3m (m=1,3,5···) are mapped on the z_1-z_2 subspace. The components on the x-y and z_1-z_2 subspaces make no contribution for the outputting torque, and the effects of the components on the z_1-z_2 subspaces can be neglected due to the isolated neutral point blocking of the current flow path on the zero-sequence subspace. By applying the VSD transformation (5) and the Park transformation (6) to Eq. (1), mathematical models of a dual three-phase PMSM can be expressed as shown in Eqs. (7-8):

$$\begin{aligned} \boldsymbol{u}_{dq}=&R_s\boldsymbol{i}_{dq}+\begin{bmatrix} L_{ls}+L_d & 0 \\ 0 & L_{ls}+L_q \end{bmatrix}p\boldsymbol{i}_{dq} \\ &+\omega\begin{bmatrix} 0 & -(L_{ls}+L_q) \\ L_{ls}+L_d & 0 \end{bmatrix}\boldsymbol{i}_{dq}+\omega\begin{bmatrix} 0 \\ \psi_f \end{bmatrix} \end{aligned} \tag{7}$$

$$\boldsymbol{u}_{xy}=R_s\boldsymbol{i}_{xy}+L_{ls}p\boldsymbol{i}_{xy} \tag{8}$$

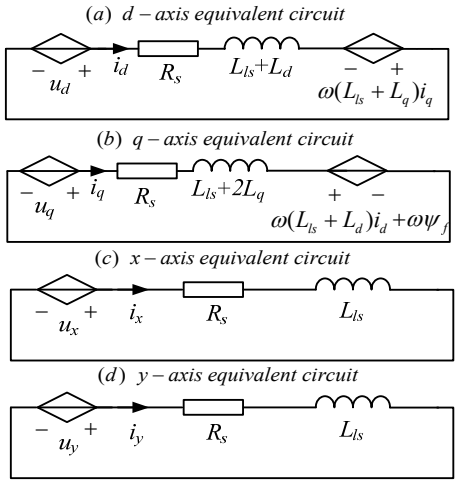

Fig. 2. Equivalent circuits of a dual three-phase PMSM drive in the VSD frame.

where ω is electrical angular speed, and L_d=3(L_{sm}–L_{rm}) and L_q=3(L_{sm}+L_{rm}). The electromagnetic torque equation can be obtained in Eq. (9) according to the principle of power conversation [26]:

$$T_e=3n_p\left[\psi_f i_q+(L_d-L_q)i_d i_q\right] \tag{9}$$

where n_p is the pole pair number. Consequently, the equivalent circuits of a dual three-phase PMSM in the VSD frames are plotted in Fig. 2.

Considering the inevitable asymmetries of the drives system, they mainly include asymmetry in the stator resistance, inductance, back EMF and supply as reported in [27]. The supply asymmetry is not taken into account in this paper since it can be eliminated easily by using an appropriate PWM strategy. Consequently, the voltage equation in Eq. (1) with asymmetries can be rewritten as follows:

$$\begin{aligned} \boldsymbol{u}_s&=R_s\boldsymbol{i}_s+\boldsymbol{L}_s p\boldsymbol{i}_s+\boldsymbol{e}_s+\Delta\boldsymbol{R}_s\boldsymbol{i}_s+\Delta\boldsymbol{L}_s p\boldsymbol{i}_s+\Delta\boldsymbol{e}_s \\ &=R_s\boldsymbol{i}_s+\boldsymbol{L}_s p\boldsymbol{i}_s+\boldsymbol{e}_s+\Delta\boldsymbol{u}_s \end{aligned} \tag{10}$$

where $\Delta\boldsymbol{R}_s$, $\Delta\boldsymbol{L}_s$ and $\Delta\boldsymbol{e}_s$ are the asymmetric components of the stator resistance, stator inductance and back EMF, respectively. $\Delta\boldsymbol{u}_s$ expresses the total asymmetrical component. Based on the symmetric component method and Euler's formula, the asymmetric component can be expressed as a combination of the positive-sequence and the negative-sequence components under each of the dual three-phase frames. The positive-sequence and negative-sequence components in the polar coordinate form for each set ($\Delta u^r{}_{ACE}$ and $\Delta u^r{}_{BDF}$) can be expressed as shown in Eq. (11):

$$\begin{cases} \Delta u^r{}_{ACE}=\dfrac{1}{2}k_1U_s e^{j(\theta+\delta 1)}+\dfrac{1}{2}k_2U_s e^{-j(\theta+\delta 1)} \\ \Delta u^r{}_{BDF}=\dfrac{1}{2}k_2U_s e^{j(\theta+\delta 2)}+\dfrac{1}{2}k_4U_s e^{-j(\theta+\delta 2)} \end{cases} \tag{11}$$

where k_1, k_2, k_3 and k_4 are the coefficients depending on the

asymmetry type, U_S is the amplitude of the symmetric component, and δ_1 and δ_2 are the initial phase angles of the asymmetric components under the ACE-phase frame and the BDF-phase frame. By applying the VSD transformation and the park transformation in Eq. (11), the unbalanced components in the *d-q* frame and the *x-y* frame can be obtained in Eqns. (12-13).

$$\begin{bmatrix}\Delta u_d\\ \Delta u_q\end{bmatrix}=\begin{bmatrix}K_d+Q_d(2\theta)\\ K_q+Q_q(2\theta)\end{bmatrix}=\frac{U_S}{2}\times \begin{Bmatrix}(k_1\cos\delta_1+k_3\cos\delta_2)+\left[k_2\cos(2\theta+\delta_1)+k_4\cos(2\theta+\delta_2)\right]\\ (k_1\sin\delta_1+k_3\sin\delta_2)-\left[k_2\sin(2\theta+\delta_1)+k_4\sin(2\theta+\delta_2)\right]\end{Bmatrix} \tag{12}$$

$$\begin{bmatrix}\Delta u_x\\ \Delta u_y\end{bmatrix}=\begin{bmatrix}Q_x(\theta)\\ Q_y(\theta)\end{bmatrix}=\frac{U_s}{2}\times \begin{Bmatrix}(k_1+k_2)\cos(\theta+\delta_1)-(k_3+k_4)\cos(\theta+\delta_2)\\ -(k_1-k_2)\sin(\theta+\delta_1)+(k_3-k_4)\sin(\theta+\delta_2)\end{Bmatrix} \tag{13}$$

Furthermore, the equivalent circuits of a dual three-phase PMSM considering asymmetry can be obtained in Fig. 3.

From the equivalent circuits in Fig. 3, it can be seen that the asymmetry causes an additional fundamental current component on the *x-y* subspace, and a DC component and second order component on the *d-q* subspace. The asymmetric current components on the *d-q* subspace cause torque ripple, and the asymmetric current components on the *x-y* subspace cause additional copper loss. A mitigation strategy for asymmetric currents will be presented in Section V.

III. DT-SVM FOR NPC-3L SIX-PHASE INVERTERS

The proposed dual three-phase space vector modulation (DT-SVM) strategy for NPC-3L six-phase inverters actually comprises two sets of three-phase SVM modules. The voltage vectors of the two sets of three-phase inverters can be defined as follows:

$$\boldsymbol{U}_1=\frac{2}{3}(u_{AM}e^{j0}+u_{CM}e^{j\frac{2\pi}{3}}+u_{EM}e^{j\frac{4\pi}{3}}) \tag{14}$$

$$\boldsymbol{U}_2=\frac{2}{3}(u_{BM}e^{j\frac{\pi}{6}}+u_{DM}e^{j\frac{5\pi}{6}}+u_{FM}e^{j\frac{3\pi}{2}}) \tag{15}$$

where u_{xM}=S_xU_{dc}/2（x=A~F）is the pole voltage of the x phase and S_x (–1, 0, 1,) are the level states of the x phase. The states of S_x can also be expressed by the symbols N, O and P, respectively. Accordingly, a vector diagram of the polar voltage for NPC-3L six-phase inverters is presented in Fig. 4(a). Furthermore, a vector diagram of the line voltage is presented in Fig. 4(b), where the symbols "+" and "–" represent the voltage values U_{dc} and $-U_{dc}$, respectively. As shown in Fig. 4, the black lines correspond to the voltage vector diagram of the ACE-phase inverter and the blue lines correspond to the voltage vector diagram of the BDF-phase

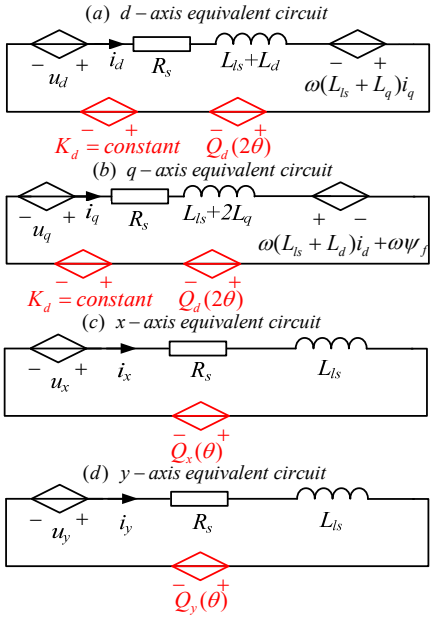

Fig. 3. Equivalent circuits of a dual three-phase PMSM under the VSD frame considering asymmetry.

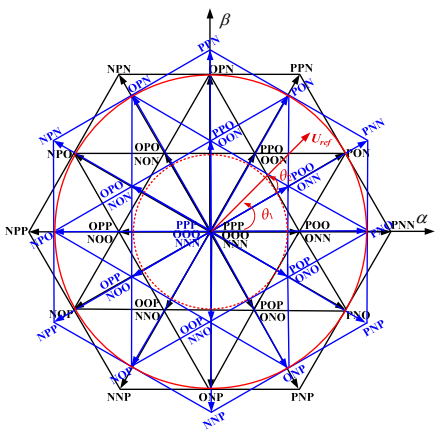

(a)

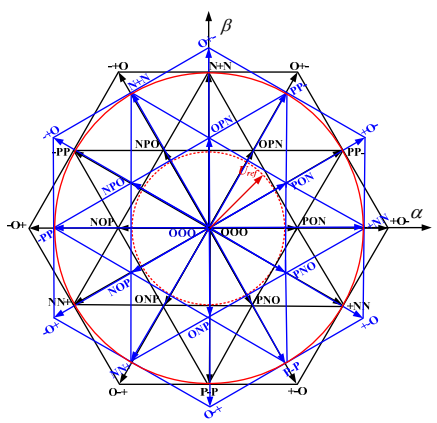

(b)

Fig. 4. Voltage vectors diagrams for the NPC-3L six-phase inverters of the DT-SVM strategy: (a) pole voltage vectors diagram; (b) line voltage vector diagram.

TABLE I
VOLTAGE VECTORS CATEGORIES FOR THE NPC-3L SIX-PHASE INVERTER OF THE DT-SVM STRATEGY

Classes	Number	Length	Vectors
Large vectors	6	$2U_{dc}/3$	PNN/PPN/NPN/ NPP/NNP/PNP/
Medium vectors	6	$\sqrt{3}U_{dc}/3$	PON/OPN/NPO/ NOP/ONP/PNO
Small vectors	12	$U_{dc}/3$	POO/ONN/PPO/ OON/OPO/NON/ OPP/NOO/OOP/ NNO/POP/ONO/
Zero vectors	3	0	OOO/PPP/NNN

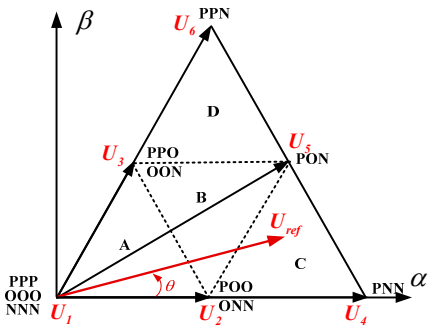

Fig. 5. Sector I of the vector diagram in the ACE-phase inverter.

inverter. Both of the dual vector diagrams comprise 27 voltage vectors, which consist of 19 effective vectors and 8 redundant vectors. The 19 effective vectors divide each of the dual vector diagrams on 6 large sectors. Each of the large sectors is further divided into 4 subsectors. In term of the differences in vector lengths, the total 27 vectors can be classified into 4 categories containing large vectors, medium vectors, small vectors and zero vectors, as shown in Table I.

In Fig. 4, it is observed that the DT-SVM vector diagram consist of two sets of NPC-3L three-phase vectors diagrams shifted by 30 degrees. The modulation processes of the two sets of three-phase vectors diagrams are similar. When the reference voltage $\boldsymbol{U}_{ref}$ on the α-β subspace is determined, the reference voltages for the modulation in two sets are obtained as shown in Eq. (16):

$$\begin{cases} \boldsymbol{U}_{1ref} = U_{ref}\angle\theta \\ \boldsymbol{U}_{2ref} = U_{ref}\angle(\theta - 30^\circ) \end{cases} \tag{16}$$

where U_{ref} is the amplitude of the reference voltage vector in the α-β subspace, $\boldsymbol{U}_{1ref}$ is the reference voltage vector in the vector diagram of the ACE-phase inverter, and $\boldsymbol{U}_{2ref}$ is the reference voltage vector in the vector diagram of the BDF-phase inverter.

For example, in sector 1 of the ACE-phase vector diagram, the subsectors of sector 1 are referred to as A, B, C and D. The nearest three vectors (NTV) around the reference voltage vector vertex are selected for synthesizing the reference voltage vector $\boldsymbol{U}_{ref}$. As shown by the location of the reference vector in Fig. 5, the NTV are $\boldsymbol{U}_2$, $\boldsymbol{U}_4$ and $\boldsymbol{U}_5$.

TABLE II
7-SEGMENT VECTOR OPERATION SEQUENCES IN SECTOR 1

Time \ Subsectors	A	B	C	D
t_1	POO	POO	POO	PPO
t_2	OOO	PON	PON	PPN
t_3	OON	OON	PNN	PON
t_4	ONN	ONN	ONN	OON
t_5	OON	OON	PNN	PON
t_6	OOO	PON	PON	PPN
t_7	POO	POO	POO	PPO

Consequently, the voltage utilization factor is defined as $H = U_{ref}/U_{dc}$ and the modulation depth is defined to be $M = \sqrt{3}U_{ref}/U_{dc}$. According to the volt-second balance principle in Eq. (17), the vectors operation time of the NTV for the synthesizing reference voltage vector can be obtained as (18).

$$\begin{cases} \boldsymbol{U}_2 T_{U2} + \boldsymbol{U}_4 T_{U4} + \boldsymbol{U}_5 T_{U5} = \boldsymbol{U}_{1ref} T_s \\ T_{U2} + T_{U4} + T_{U5} = T_s \end{cases} \tag{17}$$

$$\begin{bmatrix} T_{U2} \\ T_{U4} \\ T_{U5} \end{bmatrix} = \begin{bmatrix} 2T_s - 2\sqrt{3}HT_s\sin(\theta + 60^\circ) \\ 2\sqrt{3}HT_s\sin(60^\circ - \theta) - T_s \\ 2\sqrt{3}HT_s\sin(\theta) \end{bmatrix} \tag{18}$$

where T_{U2}, T_{U4} and T_{U5} are the vectors operation times of $\boldsymbol{U}_2$, $\boldsymbol{U}_4$ and $\boldsymbol{U}_5$, respectively, and T_s is the time of the switching period.

The 7-segment symmetric vector operation sequence is used, which takes full advantage of the redundant voltage vectors of the NTV. The 7-segment vector operation sequences in sector 1 are presented in Table II, where t_1=t_7=T_1/4, t_2=t_6=T_2/2, t_3=t_5=T_3/2 and t_4=T_1/2. In addition, T_1, T_2 and T_3 are the dwelling times of the selected voltage vectors.

The location judgment of the reference voltage vector consists of the judgment of the sector and the judgment of the subsector. The per unit value of the reference voltage vector is defined as $\boldsymbol{U}_{ref.pu}$=$\boldsymbol{U}_{ref}/U_{dc}$. In addition, $\boldsymbol{U}_{ref.pu}$ can be written in the polar coordinate form and the plural form as shown in Eq. (19). According to the range of θ, the sector number of the reference voltage vector can be easily obtained. The subsector number can be determined in term of the judgmental principle listed in Table III.

$$\begin{cases} \boldsymbol{U}_{ref.pu} = U_{ref.pu}\angle\theta \\ \boldsymbol{U}_{ref.pu} = U_{\alpha.pu} + jU_{\beta.pu} \end{cases} \tag{19}$$

IV. DC LINK CAPACITORS VOLTAGE BALANCING CONTROL

The impacts of different vector categories for the middle voltage of DC link capacitors are different. The impacts of those vectors are summarized as: (1) large vectors and zero

TABLE III
JUDGMENTAL PRINCIPLE TO DETERMINE SUBSECTORS OF THE REFERENCE VOLTAGE VECTOR

Judgment principles	Subsectors
$\sqrt{3}U_{\alpha.pu}+U_{\beta.pu}<H/\sqrt{3}$	A
$\sqrt{3}U_{\alpha.pu}-U_{\beta.pu}\geq H/\sqrt{3}$	C
$U_{\beta.pu}\geq\sqrt{3}H/6$	D
Else	B

vectors have no effect on the mid-point voltage; (2) medium vectors cause fluctuations of the mid-point voltage, which cannot be controlled by a modulation strategy; (3) small vectors, appearing in pairs, have the opposite effects on the mid-point voltage [28]. For example, the positive small vector PPO has the trend of raising the mid-point voltage, and the negative small vector OON has the trend of lowering the mid-point voltage. Hence, the DC-link mid-point voltage can be balanced by dynamically adjusting the dwelling time of the redundant small vectors. The balancing factor λ is introduced to distribute the dwelling time of the redundant small vectors in Table II.

$$\begin{cases} t_1 = t_7 = (1+\lambda)T_1/4 \\ t_4 = (1-\lambda)T_1/2 \end{cases} \tag{20}$$

Thus, the factors resulting in fluctuations of the mid-point voltage can be concluded to be: (1) the modulation depth M, which mainly determines the dwelling time of the medium vectors and small vectors; (2) the loading current I, which determines the current value flowing on the mid-point of the DC link; (3) the loading power factor, pf, which determines the direction of the current flow on the mid-point of the DC link; (4) the upper and lower capacitor values C in the DC link; and (5) the balancing factor λ, which is the only adjusting factor for balancing the mid-point voltage in the DC link. Consequently, the voltage difference between the upper capacitor and lower capacitor in the DC link is expressed as follows.

$$\Delta U_c = \frac{I_{pu}}{C_{pu}} f(M, pf, \lambda) \tag{21}$$

where I_{pu} is the per unit value of the load current amplitude, and the rated value is 10A. C_{pu} is the per unit value of the DC link capacitors C, and the value is 1000 uF. Actually, the expression $f(M, pf, \lambda)$ is a highly nonlinear function, which is very difficult to express with a time-domain expression. Some research have studied the relationships between ΔU_c and M, and pf and λ. In [28], a new model in the d-q coordinate frame is proposed to describe the expression of the middle current with a complicated piecewise function, which indirectly reflects middle voltage of the DC link. In [29], the equivalent circuit of a NPC-3L inverter is modelled

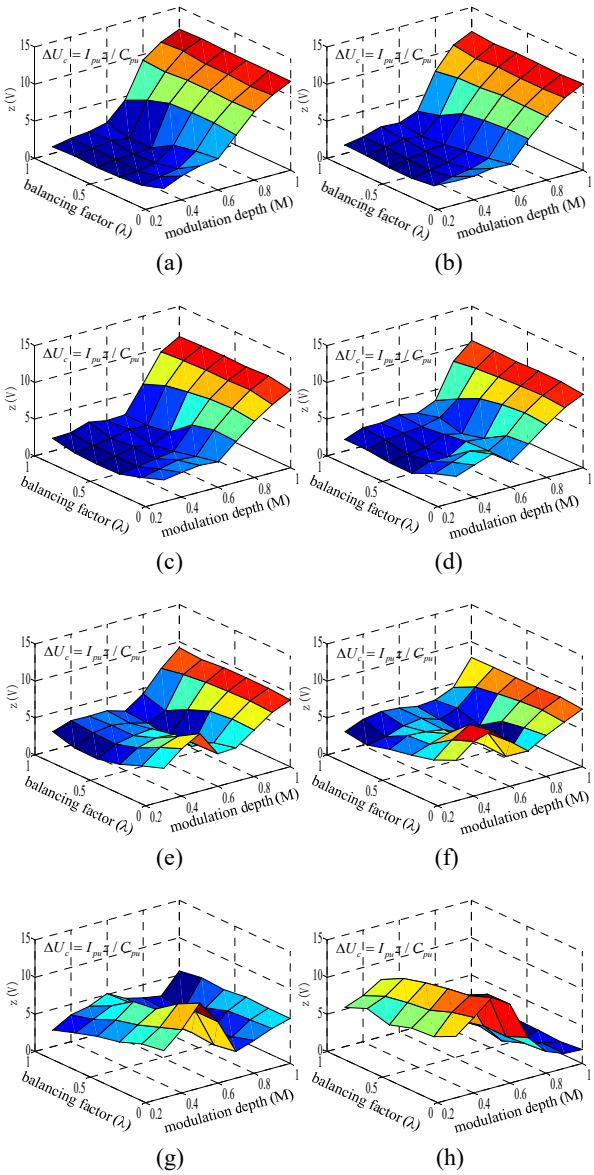

Fig. 6. Numerical fitting surface of the voltage difference between the upper capacitor and the lower capacitor: (a) load character pf=0.3; (b) load character pf=0.4; (c) load character pf=0.5; (d) load character pf=0.6; (e) load character pf=0.7; (f) load character pf=0.8; (g) load character pf=0.9; and (h) load character pf=1.0.

and the middle voltage expression is derived with the Laplace-domain. However, in engineering applications, these complicated expressions are seldom done by digital controllers like a DSP. In this paper, an effective method is proposed based on a numerical simulation. The expression Eq. (21) is discretised into several values by a numerical simulation with Matlab/Simulink, and they are saved in the memory of the controller. With allowable deviations of the middle voltage, the loading current I, the loading power factor pf and the modulation depth M, the appropriate balancing factor λ can be obtained by an interpolation approach based on the discrete values of Eq. (21). Fig. 6

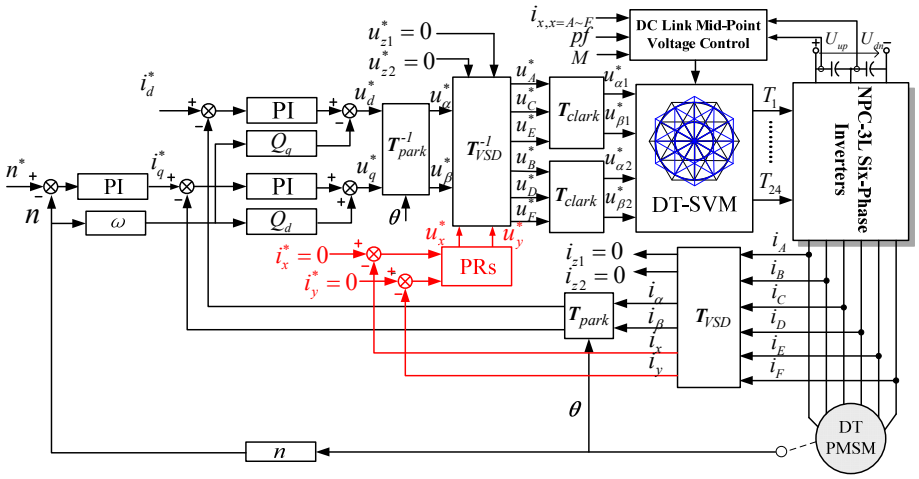

Fig. 7. Proposed control block diagram of NPC-3L six-phase inverter fed dual three-phase PMSM drives considering asymmetric factors.

presents the interpolation fitting surface of Eq. (21).

As shown in Fig. 6, some valuable conclusions can be obtained to guide in the selection of an appropriate balancing factor λ for minimizing mid-point voltage fluctuations: (1) with the same balancing factor λ, a high modulation index benefits the balancing of the DC link mid-point voltage with a high power factor *pf* in the load. On the other hand, a low modulation index has a lower DC link mid-point voltage with a low power factor in the load. (2) For medium and low modulation indexes, an appropriate increase of the balancing factor λ can suppress mid-point voltage fluctuations. However, an excessive increasing of λ aggravates the mid-point voltage fluctuations. (3) For a high modulation index, the balancing factor λ loses controllability of the mid-point voltage in the DC link.

V. CONTROL SCHEME

Based on the aforementioned VSD model of a dual three-phase PMSM, the torque component can be controlled in the *d-q* subspace, and the asymmetric component can be suppressed in the *x-y* subspace. Furthermore, the modulation of reference voltage and balancing control of the mid-point voltage can be implemented by the DT-SVM strategy. Fig. 7 presents a block diagram of the vector control for NPC-3L six-phase inverter fed dual three-phase PMSM drives by considering asymmetric factors.

As shown in Fig. 7, the outer speed controller generates the *q*-axis current reference, and the *d*-axis current reference is kept zero for the zero d-axis current (ZDC) operation. The inner current controller in the *d-q* subspace adopts PI control to generate the *d*-axis and *q*-axis voltage references, namely u_d^* and u_q^*. The feedforward compensation terms $Q_d = \omega(L_d + L_{ls})i_d + \omega\psi_f$ and $Q_q = \omega(L_q + L_{ls})i_q$ are added to the *q*-axis and *d*-axis current controllers for decoupling the interactions between the *d*-axis and *q*-axis. Thus, the dynamic performance of the drive system can be improved. The bandwidths of the *d*-axis and *q*-axis PI current controllers are designed slightly larger than twice the fundamental frequency (2ω). Therefore, the oscillating terms $Q(2\theta)$ in Fig. 3(a) and Fig. 3(b) can be effectively controlled. Then applying the transformation matrix $\boldsymbol{T}_{park}^{-1}$ to the voltage references vector $[u_d^*, u_q^*]^{\mathrm{T}}$, the voltage references u_α^* and u_β^* are obtained. $\boldsymbol{T}_{park}^{-1}$ is the inverse matrix of $\boldsymbol{T}_{park}$ in Eq. (6).

Meanwhile, the inner current controller in the *x-y* subspace adopts a proportional resonant (PR) controller for controlling the *x*-axis and *y*-axis currents to be zero. Then the voltage references u_x^* and u_y^* are obtained. The transfer function of the PR controllers in Fig.7 is given as follows:

$$G(s) = K_p + \frac{2K_r\omega_c s}{s^2 + 2\omega_c s + \omega^2} \tag{22}$$

where K_p and K_r are the proportional and resonant coefficients, respectively, ω is the fundamental frequency, and ω_c is the cut-off frequency, which is helpful for reducing the sensitivity to slight frequency oscillations of the fundamental frequency. A smaller ω_c makes the PR controllers more sensitive to frequency variations and lead to a slower transient response. The value of ω_c is chosen to be 0.02 times the fundamental frequency in this paper, which is based on the better experimental performance in Section VI. The z transformation makes it easier to execute Eq. (22) by a DSP, and the z transformation expression of Eq. (22) is presented as follows:

$$G(z) = K_p z^0 + \frac{2K_r\omega_c z^0 - 2K_r\omega_c e^{-\omega_c T}\left[\cos(\Delta\times T) + \frac{\omega_c}{\Delta}\sin(\Delta\times T)\right]z^{-1}}{1 - 2e^{-\omega_c T}\cos(\Delta\times T)z^{-1} + e^{-2\omega_c T}z^{-2}} \tag{23}$$

where $\Delta = \sqrt{\omega^2 - \omega_c^2}$, and T is the control period in the DSP.

TABLE IV
MAIN PARAMETERS IN THE EXPERIMENTS

Name	Value
Pole pair number n_p	3
Stator resistance R_p	0.4 Ω
PM flux (peak) ψ_f	0.31 Wb
q-axis inductance L_q	8.71 mH
d-axis inductance L_d	5.68 mH
Experimental speed	550 rpm
DC voltage U_{dc}	115 V
Switching frequency	5 kHz
Balancing factor λ	0.9
Load type	Generator

Furthermore, by multiplying the inverse transformation of $\boldsymbol{T}_{VSD}$ to the voltage references vector $[u_\alpha^*, u_\beta^*, u_x^*, u_y^*, u_{z1}^* = 0, u_{z2}^* = 0]$, the voltage references on the natural frames, namely u_x (x=A~F) are obtained. Then with a Clark transform, the voltage references $u_{\alpha 1}^*$ and $u_{\beta 1}^*$ are provided for the first three-phase NPC-3L inverter, and the voltage references $u_{\alpha 2}^*$ and $u_{\beta 2}^*$ are provided for the second inverter. The Clark transform matrix $\boldsymbol{T}_{clark}$ is given in Eq. (24).

$$\boldsymbol{T}_{clark} = \frac{2}{3}\begin{bmatrix} 1 & -1/2 & -1/2 \\ 0 & \sqrt{3}/2 & -\sqrt{3}/2 \end{bmatrix} \tag{24}$$

The switching signals are generated with the modulation strategy in Section III and the balancing factor λ in Section IV.

VI. EXPERIMENTAL VERIFICATION

A laboratory experimental platform of a NPC-3L inverter fed dual three-phase PMSM drive is built to verify the validity of the presented analysis and control scheme considering asymmetric factors. The control part consists of a DSP (TMS-F28335) and a FPGA (Xinlix-Spartan6), which are used to implement the control algorithms and switching strategies, respectively. The power conversion circuit is constructed by IGBT models (F3L100R07W2E3-B11). A PM machine feeding the resistors is coupled to the tested dual three-phase PMSM machine for providing a load. The system parameters of the experiments are given in Table IV.

Fig. 8 shows measured steady-state waveforms of dual three-phase PMSM drives without using closed-loop current control in the x-y subspace. Due to the inevitable differences in the parameters of the dual three-phase windings, the phase currents show slight difference in the waveforms of i_A and i_B as shown in Fig. 8(a). Thus, the unbalanced components cause a fundamental-frequency component with a peak value of about 0.4A in the x-y subspace as shown in Fig. 8(b). Fig.

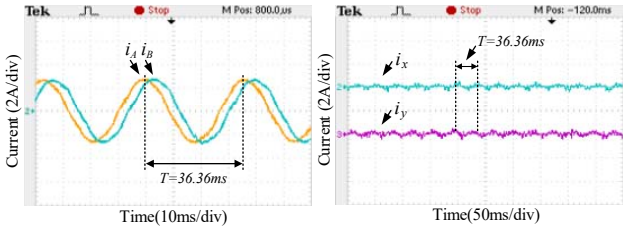

(a) (b)

Fig. 8. Measured steady-state waveforms with the open-loop control in the x-y subspace: (a) A-phase and B-phase currents; (b) phase current components in the x-y subspace.

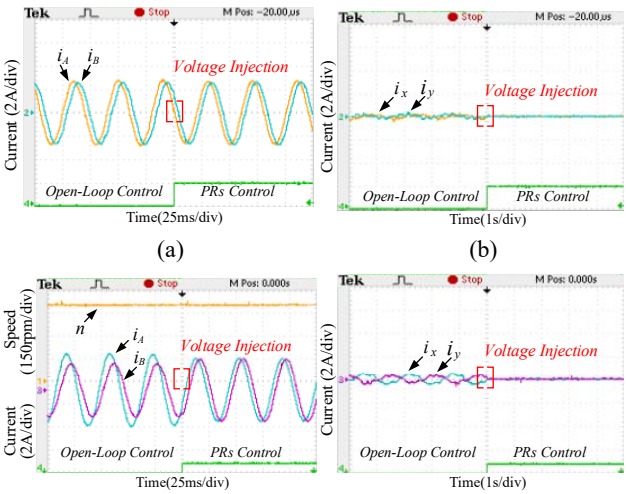

(a) (b)

(c) (d)

Fig. 9. Measured transient performance of the proposed PR based controller in the x-y subspace: (a) phase A and phase B currents; (b) harmonic current components in the x-y subspace; (c) phase A and phase B currents while connecting a 5mH inductor to phase B; and (d) current components in the x-y subspace while connecting a 5mH inductor to phase B.

9 shows the performance when a closed-loop current controller is added to the x-y subspace. As mentioned in Section V, the closed-loop current controller can eliminate the fundamental current component in the x-y subspace in such a way that the asymmetry of the phase currents in the dual three-phase windings can be mitigated. Fig. 9(a) shows that the slight differences in the phase currents of dual the three-phase windings are effectively removed, and Fig. 9(b) shows that the fundamental current components in the x-y subspace are effectively eliminated. Furthermore, an additional 5mH inductor is connected to the B phase. Therefore, the asymmetry issue becomes aggravated. Fig. 9(c) and (d) verify that the proposed closed-loop current control in the x-y subspace are still effective in suppressing unbalanced phase currents by eliminating the current components in the x-y subspace.

Secondly, measured steady-state waveforms of a dual three-phase PMSM drive base on the proposed control diagram are presented in Fig. 10. The load torque is 7.46 Nm and the operation speed is stably controlled at 550 rpm as

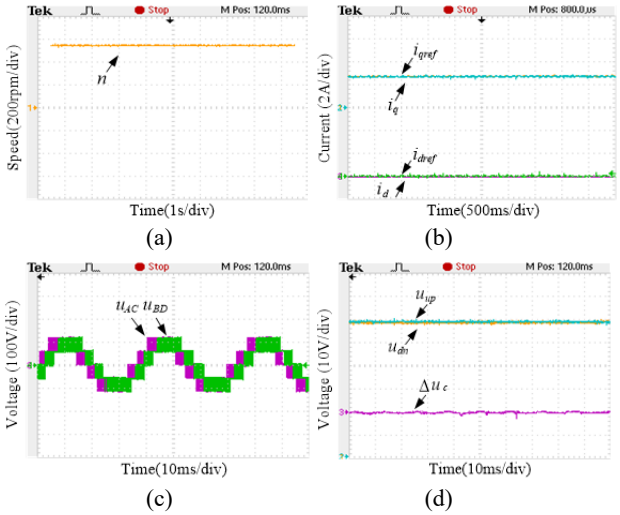

Fig. 10. Measured steady-state waveforms of a dual three-phase PMSM drive with the proposed control scheme: (a) rotor speed; (b) *d-q* axis reference currents and measured currents, (c) line voltages (AC, BD); (d) DC capacitor voltages and the voltage difference between the upper and the lower capacitors.

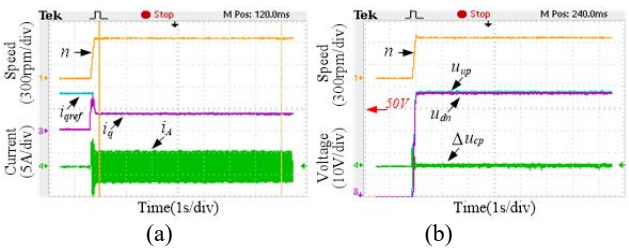

Fig. 11. Measured transient performance of the drive of the proposed control scheme during the starting process: (a) rotor speed, q-axis current and phase-A current; (b) rotor speed, DC capacitor voltages and voltage difference between the upper and lower capacitors in the DC link.

shown in Fig. 10(a). Fig. 10(b) shows measured steady-state waveforms of the *d-q* axis reference currents and measured currents. The actual currents can accurately track their reference values. The waveforms of the line-to-line voltages (AC, BD) present five-level states with a 30-degree shifted angle as shown in Fig. 10(c). Fig. 10(d) presents waveforms of the DC capacitor voltages and the mid-point voltage deviation in the DC link. This indicates that the difference between the upper and lower capacitor voltages is less than 5% U_{dc}.

Thirdly, the measured dynamic performance of the proposed control scheme for dual three-phase PMSM drives during the starting process is plotted as shown in Fig.11. The motor speed goes from 0 rpm to 550 rpm and the q-axis current tracks the reference current accurately and rapidly as shown in Fig. 11(a). The upper and lower capacitor voltages in the DC link are balanced well during the dynamic process as shown in Fig. 11(b). Furthermore, Fig. 12 shows the measured dynamic performance of the drive when the operation speed is changed, where the machine speed

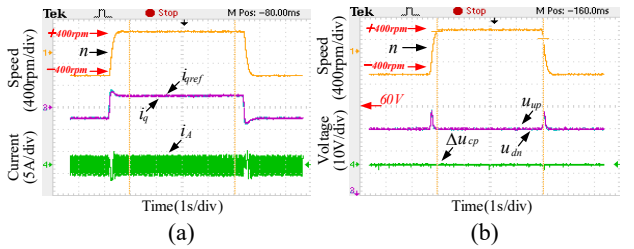

Fig. 12. Measured dynamic performance of the drive of the proposed control scheme under change in speed: (a) rotor speed, q-axis current and phase-A current; (b) rotor speed, DC capacitor voltages and voltage difference between the upper and lower capacitors in the DC link.

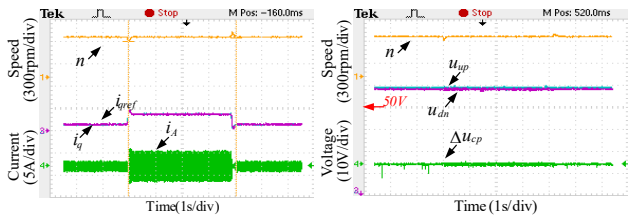

Fig. 13. Measured dynamic performance of the drive of the proposed control scheme under a change in load: (a) rotor speed, q-axis current and phase A current; (b) rotor speed, DC capacitor voltages and voltage difference between the upper and lower capacitors in the DC link.

increases from -400 rpm to 400 rpm, and then decreases back to -400 rpm. As shown in Fig. 12(a), the measured q-axis current still tracks the reference current accurately and rapidly. The upper and lower capacitor voltages of the DC link are also balanced well in the dynamic process in Fig.12 (b). Fig. 14 shows the measured dynamic performance of the drive with a change in the load, where the torque is changed between 2.21 Nm and 7.46 Nm. In addition, the q-axis current can track the reference current accurately and rapidly in Fig. 13(a), and the DC link capacitor voltages are balanced well in Fig. 13(b).

Fourthly, the measured performance of the decoupling effects of the current controller is verified as shown in Fig. 14. This verifies the validity of the feed-forward compensation for improving the dynamic performance of the drive, where the machine speed is 500 rpm. As shown in Fig. 14(a), there exists a slight disturbance in the d-axis current when the q-axis current is suddenly changed without the decoupling control. On the other hand, the d-axis and q-axis currents are decoupled well in Fig. 14(b) by adopting the decoupling control in the proposed control scheme.

Finally, Fig. 15 shows experiments based on NPC-3L six-phase inverter fed *RL* loads to verify the correctness of the numerical fitting surface in Fig. 6. For showing the effects of the balancing factor and modulation depth, the loading current and *pf* are kept constant at 2.42 A (rms) and 0.8, respectively. The DC link capacitor value is 2000 uF. Thus, the per unit values of the load current and DC link capacitor

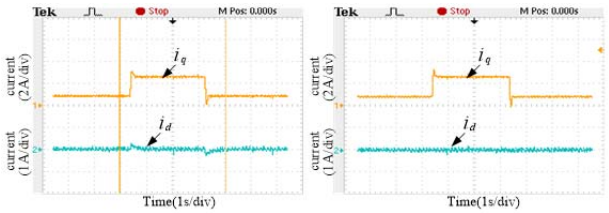

Fig. 14. Measured performance of the feed-forward compensation: (a) *d-q* axis current responses without the decoupling control; (b) *d-q* axis current responses with the decoupling control.

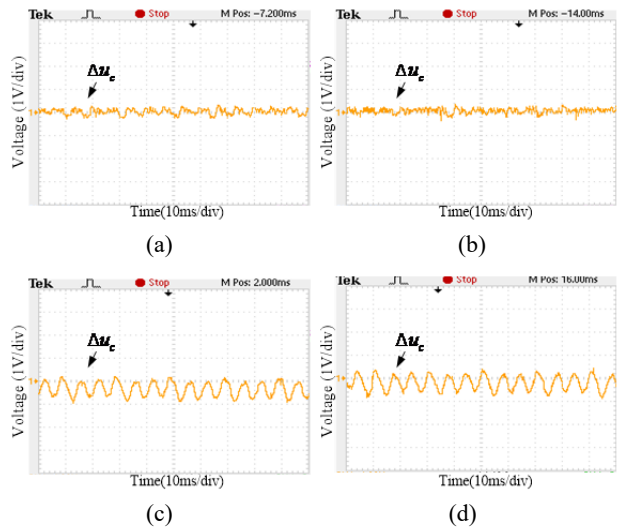

Fig. 15. Measured voltage difference between the upper and lower capacitors with *pf*=0.8: (a) *M*=0.75 and λ=0.5; (b) *M*=0.75 and λ=1.0; (b) *M*=1.0 and λ=0.5; and (b) *M*=1.0 and λ=1.0.

are I_{pu}=0.3422 and C_{pu}=2. As shown in Fig. 15(a) and Fig. 15(b), the modulation depth *M* is 0.75, and the values of λ are 0.5 and 1.0, respectively. The values of Δu_c are around 0.6V and 0.65V. Using the equation $z(\mathrm{V}) = \Delta u_c C_{pu} / I_{pu}$, the values of z(V) can be calculated as 3.51 and 3.80, respectively. These values agree with the corresponding values in Fig.6 (f). Similarly, when *M* is 1.0, and the values of λ are 0.5 and 1.0 in Fig. 15(c) and Fig. 15(d), the values of z(V) are calculated at around 7.10 and 7.60, respectively. These values are also approximately equal to the corresponding values in Fig. 6(f). In addition, Fig. 15(c) and Fig. 15(d) also verify the aforementioned conclusion that the balancing factor λ has less controllability in terms of mid-point voltage in the DC link for a high value of *M*.

VII. Conclusions

This paper has studied the modelling, modulation strategy and control scheme for NPC-3L inverter fed dual three-phase PMSM drives. The key is to deduce the VSD models of the dual three-phase PMSM with asymmetric factors, and to design the DT-SVM strategy for the NPC-3L inverter. Then the control scheme is proposed for drives based on the VSD models and the DT-SVM strategy. According to the control scheme, the torque component is controlled in the *d-q* subspace, and the unbalanced currents are suppressed to zero in the *x-y* subspace by using the PRs control. The upper and lower capacitor voltages in the DC link are balanced well during various operation conditions by selecting an appropriate balancing factor with the DT-SVM. Experiments on a laboratory setup have been presented to demonstrate the validity of the proposed control scheme for NPC-3L inverter fed dual three-phase PMSM drives.

Acknowledgment

This work was supported in part by the National Key Basic Research Program of China (973 program) under Grant 2013CB035603, and in part by National Natural Science Foundation of China under Grant 51577027, and in part by the Fundamental Research Funds for the Central Universities.

References

[1] T. M. Jahns, “Improved reliability in solid-state AC drives by means of multiple independent phase-drive units,” *IEEE Trans. Ind. Appl.*, Vol. 16, No. 3, pp. 321-331, May 1980.

[2] A. R. Munoz, “Dual stator winding induction machine drive,” *IEEE Trans. Ind. Appl.*, Vol. 36, No. 5, pp. 1369-1379, Sep./Oct. 2000.

[3] E. Levi, R. Bojoi, F. Profumo, H. A. Toliyat, and S. Williamson, “Multiphase induction motor drives – A technology status review,” *IET Electric Power Appl.*, Vol. 1, No. 4, pp. 489-516, Jul. 2007.

[4] X. Wang, Z. Wang, M. Cheng, and Y. Hu, “Remedial strategies of T-NPC three-level asymmetric six-phase PMSM drives based on SVM-DTC,” *IEEE Trans. Ind. Electron.*, Vol. 64, No. 9, pp. 6841-6853, Sep. 2017.

[5] L. Alberti and N. Bianchi, “Experimental tests of dual three-phase induction motor under faulty operating condition,” *IEEE Trans. Ind. Electron.*, Vol. 59, No. 5, pp. 2041-2048, May 2012.

[6] R. H. Nelson and P. C. Krause, “Induction machine analysis for arbitrary displacement between multiple winding sets,” *IEEE Trans. Power App. Syst.*, Vol. PAS-93, No. 3, pp. 841-848, May 1974.

[7] M. A. Abbas, R. Christen, and T. M. Jahns, “Six-phase voltage source inverter driven induction motor,” *IEEE Trans. Ind. Appl.*, Vol. IA-20, No. 5, pp. 1251-1259, Sep. 1984.

[8] R. Bojoi, M. Lazzari, F. Profumo, and A. Tenconi, “Digital field-oriented control for dual three-phase induction motor drives,” *IEEE Trans. Ind. Appl.*, Vol. 39, No. 3, pp. 752-760, May/Jun. 2003.

[9] F. Yuan and S. Huang, “A hybrid current controller for dual three-phase permanent magnet synchronous motors,” *IEEJ Trans. Electr. Electron. Eng.*, Vol. 9 No. 2, pp. 214-218, Jan. 2014.

[10] Y. Zhao and T. A. Lipo, “Space vector PWM control of dual three-phase induction machine using vector space decomposition,” *IEEE Trans. Ind. Appl.*, Vol. 31, No. 5, pp. 1100-1109, Sep./Oct. 1995.

[11] R. Bojoi, E. Levi, F. Farina, A. Tenconi, and F. Profumo, "Dual three-phase induction motor drive with digital current control in the stationary reference frame," *IEE Proceedings - Electric Power Applications,* Vol. 153, No. 1, pp. 129-139, Jan. 2006.
[12] J. Karttunen, S. Kallio, P. Peltoniemi, P. Silventoinen, and O. Pyrhönen, "Decoupled vector control scheme for dual three-phase permanent magnet synchronous machines," *IEEE Trans. Ind. Electron.*, Vol. 61, No. 5, pp. 2185-2196, May 2014.
[13] H. S. Che, E. Levi, M. Jones, W. P. Hew, and N. A. Rahim, "Current control methods for an asymmetrical six-phase induction motor drive," *IEEE Trans. Power Electron.*, Vol. 29, No. 1, pp. 407-417, Jan. 2014.
[14] Y. Hu, Z. Q. Zhu, and K. Liu, "Current control for dual three-phase permanent magnet synchronous motors accounting for current unbalance and harmonics," *IEEE J. Emerg. Sel. Topics Power Electron.,* Vol. 2, No. 2, pp. 272-284, Jun. 2014.
[15] R. Bojoi, F. Farina, G. Griva, F. Profumo, and A. Tenconi, "Direct torque control for dual three-phase induction motor drives," *IEEE Trans. Ind. Appl.*, Vol. 41, No. 6, pp. 1627-1636, Nov./Dec. 2005.
[16] K. Hatua and V. T. Ranganathan, "Direct torque control schemes for split-phase induction machine," *IEEE Trans. Ind. Appl.* Vol. 41, No. 5, pp. 1243-1254, Sep./Oct. 2005.
[17] K. D. Hoang, Y. Ren, Z. Q. Zhu, and M. Foster, "Modified switching-table strategy for reduction of current harmonics in direct torque controlled dual-three-phase permanent magnet synchronous machine drives," *IET Electr. Power Appl.*, Vol. 9, No. 1, pp. 10-19, Jan. 2015.
[18] F. Barrero, M. R. Arahal, R. Gregor, S. Toral, and M. J. Duran, "One-step modulation predictive current control method for the asymmetrical dual three-phase induction machine," *IEEE Trans. Ind. Electron.*, Vol. 56, No. 6, pp. 1974-1983, Jun. 2009.
[19] M. J. Duran, J. Prieto, F. Barrero, and S. Toral, "Predictive current control of dual three-phase drives using restrained search techniques," *IEEE Trans. Ind. Electron.*, Vol. 58, No. 8, pp. 3253-3263, Aug. 2011.
[20] R. Gregor, F. Barrero, S. L. Toral, M. J. Duran, M. R. Arahal, J. Prieto, and J. L. Mora, "Predictive-space vector PWM current control method for asymmetrical dual three-phase induction motor drives," *IET Electric Power Applications*, Vol. 4, No. 1, pp. 26-34, Jan. 2010.
[21] S. Kouro, M. Malinowski, K. Gopakumar, J. Pou, L. G. Franquelo, B. Wu, J. Rodriguez, M. A. Perez, and J. I. Leon, "Recent advances and industrial applications of multilevel converters," *IEEE Trans. Ind. Electron.*, Vol. 57, No. 8, pp. 2553-2580, Aug. 2010.
[22] A. Nabae, I. Takahashi, and H. Akagi, "A new neutral-point-clamped PWM inverter," *IEEE Trans. Ind. Appl.*, Vol. IA-17, No. 5, pp. 518-523, Sep. 1981.
[23] L. Gao and J. E. Fletcher, "A space vector switching strategy for three-level five-phase inverter drives," *IEEE Trans. Ind. Electron.*, Vol. 57, No. 7, pp. 2332-2343, Jul. 2010.
[24] O. Dordevic, M. Jones, and E. Levi, "A comparison of carrier-based and space vector PWM techniques for three-level five-phase voltage source inverters," *IEEE Trans. Ind. Inform.*, Vol. 9, No. 2, pp. 609-619, May 2013.
[25] O. Dordevic, E. Levi, and M. Jones, "A vector space decomposition based space vector PWM algorithm for a three-level seven-phase voltage source inverter," *IEEE Trans. Power Electron.* , Vol. 28, No. 2, pp. 637-649, Feb. 2013.
[26] H. Ryu, J. Kim, and S. Sul, "Synchronous-frame current control of multiphase synchronous motor under asymmetric fault condition due to open phases," *IEEE Trans. Ind. Appl.*, Vol. 42, No. 4, pp. 1062-1070, Jul./Aug. 2006.
[27] R. Bojoi, F. Farina, M. Lazzari, F. Profumo, and A. Tenconi, "Analysis of the asymmetrical operation of dual three-phase induction machines," in *Electric Machines and Drives Conference*, pp. 429-435, 2003.
[28] N. Celanovic and D. Boroyevich, "A comprehensive study of neutral-point voltage balancing problem in three-level neutral-point-clamped voltage source PWM inverters," *IEEE Trans. Power Electron.*, Vol. 15, No. 2, pp. 242-249, Mar. 2000.
[29] B. Zhang, Z. Wang, K. Chu, and M. Cheng, "Analysis of fluctuation in DC link capacitor voltage of NPC three-level inverter and its mitigation under fault tolerant control mode," *Transactions of China Electro Technical Society.*, Vol. 30, No. 7, pp. 52-61, Apr. 2015.

Jian Chen received his B.S. degree from Anhui University of Science and Technology, Huainan, China, in 2013; and his M.S. degree from Southeast University, Nanjing, China, in 2016, all in Electrical Engineering. He is an Electrical Engineer with the Shenzhen Inovance Technology Co., LTD., China, where he is presently working on the R&D of low voltage drive systems.

Zheng Wang (S'05–M'09-SM'14) received his B.S. and M.S. degrees from Southeast University, Nanjing, China, in 2000 and 2003, respectively; and his Ph.D. degree from University of Hong Kong, Hong Kong, China, in 2008, all in Electrical Engineering. From 2008 to 2009, he was a Postdoctoral Fellow at Ryerson University, Toronto, ON, Canada. He is presently working as a full Professor in the School of Electrical Engineering, Southeast University. His current research interests include electric drives, power electronics, and distributed generation. He has authored or coauthored over 80 internationally refereed papers and four books in these areas. Professor Wang has received several academic awards including an IEEE PES Chapter Outstanding Engineer Award, a Best Paper Award of the International Conference on Electrical Machines and Systems (ICMES), a Best Session Paper Award of the IEEE Annual Meeting of Industrial Electronics (IECON), and a Nanjing Outstanding Paper Award of Natural Science.

Yibo Wang received his B.S. degree in Electrical Engineering from Southeast University, Nanjing, China, in 2015, where he is presently working towards his M.S. degree. His current research interests include multilevel converters, multilevel PWM strategies, the control of multiphase permanent magnet synchronous motors, and the fault tolerant control of multiphase motors.

Ming Cheng (M'01–SM'02-F'15) received his B.S. and M.S. degrees from the Department of Electrical Engineering, Southeast University, Nanjing, China, in 1982 and 1987, respectively; and his Ph.D. degree from the Department of Electrical and Electronic Engineering, University of Hong Kong, Hong Kong, China, in 2001, all in Electrical Engineering. Since 1987, he has been with Southeast University, where he is presently working as a Distinguished Professor in the School of Electrical Engineering and as the Director of the Research Center for Wind Power Generation. From January to April 2011, he was a Visiting Professor in the Wisconsin Electric Machine and Power Electronics Consortium, University of Wisconsin, Madison, WI, USA. His current teaching and research interests include electrical machines, motor drives for EVs, and renewable energy generation. He has authored or co-authored more than 300 technical papers and four books, and is the holder of 70 patents in these areas. Professor Cheng is a Fellow of the Institution of Engineering and Technology. He has served as a Chair and as an Organizing Committee Member for many international conferences. He was a Distinguished Lecturer of the IEEE Industry Applications Society in 2015/2016.